Anomalous band renormalization due to a high-energy kink in $K_{0.65}RhO_2$ with colossal thermoelectric power factor

Susmita Changdar,[1] Grigory Shipunov,[2] Nesta B. Joseph,[3] Nicholas C. Plumb,[4] Ming Shi,[4] Bernd Büchner,[2] Awadhesh Narayan,[3] Saicharan Aswartham,[2] and Setti Thirupathaiah[1,*]

[1]*Condensed Matter Physics and Material Sciences Department, S. N. Bose National Centre for Basic Sciences, Kolkata, West Bengal-700106, India*

[2]*Leibniz Institute for Solid State Research, IFW Dresden, D-01171 Dresden, Germany*

[3]*Solid State and Structural Chemistry Unit, Indian Institute of Science, Bangalore, Karnataka-560012, India*

[4]*Swiss Light Source, Paul Scherrer Institute, CH-5232 Villigen PSI, Switzerland*

(Received 2 July 2020; accepted 21 April 2021; published 5 May 2021)

We identify highly correlated hole pocket on the Fermi surface of colossal thermoelectric material $K_{0.65}RhO_2$, studied using high-resolution angle-resolved photoemission spectroscopy (ARPES) and density-functional theory (DFT) calculations. Most importantly, two *kinks* at binding energies of 75 and 195 meV have been observed below the Fermi level. While the low-energy *kink* at 75 meV can be understood as a result of the electron-phonon interaction, the high-energy *kink* at 195 meV is a discovery of this system, leading to anomalous band renormalization, possibly originated from the bosonic excitations at higher frequencies. We further notice that the high-energy anomaly has important implications on the colossal thermoelectric power of $K_{0.65}RhO_2$.

DOI: 10.1103/PhysRevMaterials.5.055402

I. INTRODUCTION

Strong electronic correlations are vital in yielding various exotic systems such as high-T_c superconductors [1], heavy fermionic materials [2], quantum anomalous Hall insulators (QAHIs) [3], half metals [4], Mott insulators [5], itinerant magnets [6], and high-thermopower materials [7]. Electron-electron (*e*-*e*) correlations turn the materials to heavy fermionic systems, QAHIs, half metals and Mott insulators, while the electron-magnon interactions are expected to cause the itinerant ferromagnetism [8,9]. On the other hand, the electron-phonon (*e*-ph) interactions are thought to play a major role in the high-T_c superconductivity [10] and high thermoelectricity [11]

For a quite some time, the compounds of the type A_xBO_2 (A = Li, Na, and K, B = Co and Rh) have been the scientific topic of much interest due to their diverse physical properties [12–15]. Interestingly, depending on the amount of Na present in Na_xCoO_2, it exhibits superconductivity in the hydrated state for $x \approx 0.35$ [16], shows giant Seebeck coefficient for $0.7 < x < 1$ [17], possesses magnetic ordering for $x \approx 0.75$ [18,19] and charge ordering for $x \approx 0.5$ [20]. Crystal-field splitting [21], strong spin-orbit interactions [22], electron-electron [23], and electron-phonon interactions [24] are suggested for the cause of unusual physical properties. On the other hand, K_xRhO_2 a similar layered compound does not seem to be showing the physical properties as diverse as Na_xCoO_2. It was reported to show a large thermoelectric power [15,25,26], but still is half to that of Na_xCoO_2 [13], despite both showing *e*-ph interactions at a Debye frequency of 70-75 meV [27–29]. Earlier ARPES report on K_xRhO_2 hinted at the importance of electron-boson scattering for the recorded high thermopowers [29]. In this contribution, we study the effect of electronic correlation on the low-energy electronic structure of the layered $K_{0.65(2)}RhO_2$ single crystal using ultrahigh energy resolution ARPES technique and DFT calculations [30].

II. EXPERIMENTAL DETAILS

Single-crystal growth. Single crystals of K_xRhO_2 were grown from the mixtures of K_2CO_3 and Rh_2O_3. The total charge mixture of 4.5 grams was placed in an alumina crucible and heated to the 1200 °C in a box furnace, after a dwelling time of 2 hours, the furnace is slowly cooled to 950 °C and later fast-cooled to room temperature. Plate-like hexagonal-shaped single crystals were grown at the bottom of the crucible. Crystals were grown in layered morphology in hexagonal structure up to few mm^2 in size. Compositional analysis from EDX gives the phase with the stoichiometry $K_{0.65(2)}RhO_2$. As-grown single crystals were crushed and measured with powder x-ray diffraction (XRD).

ARPES measurements. ARPES measurements were performed in Swiss Light Source (SLS) at the SIS beamline using a VG-Scienta R4000 electron analyzer. The photon energy was varied between 20 and 140 eV. Overall energy resolution was set between 15 and 25 meV depending on the photon energy. The angular resolution was fixed at 0.2°. Samples were cleaved *in situ* at a sample temperature of 15 K and the chamber vacuum was better than 5×10^{-11} mbar during the measurements.

III. RESULTS AND DISCUSSION

ARPES data of $K_{0.65}RhO_2$ are shown in Fig. 1. From the Fermi-surface map shown in Fig. 1(a), we observe one nearly

*setti@bose.res.in

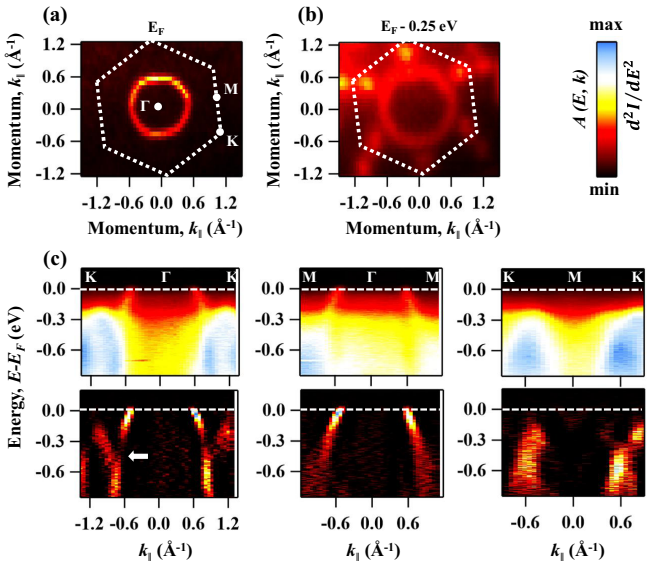

FIG. 1. ARPES measurements of $K_{0.65}RhO_2$. The data are measured using *p*-polarized light with a photon energy of 140 eV. (a) Fermi-surface map. (b) Constant energy map taken at a binding energy of 0.25 eV below E_F. (c) Energy distribution maps (EDMs) showing the band dispersions along the Γ-*K*, Γ-*M*, and *M*-*K* high-symmetry directions.

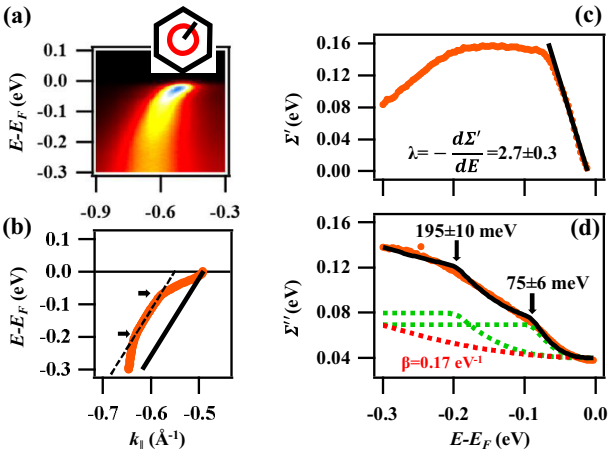

FIG. 2. (a) Energy distribution map taken along the Γ-*M* orientation as shown in the inset. (b) Band dispersion extracted by fitting the momentum distribution curves of the EDM shown in panel (a) using a Lorentzian function. Black dashed line in panel (b) is a linear fit to band dispersion at the higher binding energy within the window of (−0.2 eV, −0.09 eV). The arrows in panel (b) show the energy positions of the *kinks*. (c) Real part of the self-energy (Σ') extracted from the EDM shown in panel (a). In panel (c), the black line is linear fit to the data performed to extract the coupling constant $\lambda = 2.7 \pm 0.3$. (d) Imaginary part of the self-energy (Σ'') extracted from the EDM shown in panel (a). In panel (d), the black curve represents fitting with combined functions of Fermi-liquid theory type and Eliashberg spectral functions (see text).

circular-shaped Fermi pocket centered at Γ with a Fermi vector of $k = 0.51 \pm 0.02$ Å^{-1}. From the constant energy contour taken at a binding energy of 0.25 eV, shown in Fig. 1(b), we observe six tiny spectral sheets near six *K* points. Moreover, at this binding energy, size of the Fermi pocket centered at Γ has increased and the circular shape is turned into a hexagonal shape. Energy distribution maps (EDMs) taken along the Γ-*M*, Γ-*K*, and *K*-*M* directions [see the top panels in Fig. 1(c)] suggest that the Fermi sheet centered at Γ has a hole-like band dispersion. Further from the EDMs taken along the Γ-*K* and *K*-*M* directions, we realize that the tiny spectral sheet near the *K* point originates from another hole-like band dispersion with a band-top at 0.25 eV below E_F. This is further confirmed from the second derivative intensity (I) of the EDMs ($\frac{d^2I}{dE^2}$) as shown in the bottom panels of Fig. 1(c). Arrow on the second derivative EDM in the Γ-*K* direction indicates an antiband crossing between the two hole-like band dispersions at ≈0.4 eV below E_F. Above this binding energy, the two hole-like bands are well separated in the momentum space. Importantly, no antiband crossing is found from the second derivative EDM in the Γ-*M* direction, down to 0.8 eV of the binding energy. Next, comparing our experimental band structure with the available ARPES data on these type of systems, analogous to Na_xCoO_2 [27,28,31] and Li_xCoO_2 [32], we could also observe only one circular-shaped hole pocket from the Fermi surface map. Most importantly, in agreement with the previous report on $K_{0.62}RhO_2$ [29], we identified an antiband crossing at ≈0.4 eV below E_F in the Γ-*K* direction. Furthermore, the top of hole-like band at the *K* point is found nearly at the same binding energy of 0.25 eV. Additional comparison between our ARPES data and DFT calculations can be found in the the Supplemental Material [30].

Having thoroughly established the low-energy electronic structure of $K_{0.65}RhO_2$, experimentally, we then move on to the spectral function analysis of our experimental data. The band dispersion shown in Fig. 2(b) is extracted from the EDM of Fig. 2(a) by fitting the momentum distribution curves (MDCs) with a Lorentzian function, analogous to the spectral function

$$A(E, k) = \frac{-1}{\pi} \frac{\Sigma''}{(E_k - E_0 - \Sigma')^2 + (\Sigma'')^2}.$$

Here, $\Sigma'(E)$ and $\Sigma''(E)$ are the real and imaginary parts of the complex self-energy function defined as $\Sigma(E) = \Sigma' + i\Sigma''$. E_k is the renormalized band dispersion which is generally obtained from the ARPES measurements [see Fig. 2(b)] and E_0 is the bare band dispersion which is generally obtained by fitting the tight-binding parameters to the experimental data. Nevertheless, the bare band dispersion can also be obtained reasonably by fitting experimental data at higher binding energies where the electronic correlations are negligible. The black-dashed curve in Fig. 2(b) is one such fitting at higher binding energies. Then, the difference between E_k [orange data in Fig. 2(b)] and E_0 [solid black line in Fig. 2(b), momentum offset to the dashed black line] provides the real part of the self-energy $\Sigma'(E) = E_k - E_0$, as shown in Fig. 2(c). On the other hand, the imaginary part of the self-energy shown in Fig. 2(d) is calculated from the energy-dependent spectral width [$\Delta k(E)$], derived from the MDC fitting, multiplied by the renormalized Fermi velocity ($v_F = 0.6$ eV Å), $\Sigma'' = \Delta k(E) v_F$.

Most interestingly, we observe two *kinks* from the band dispersion shown in Fig. 2(b). These *kinks* have direct implications on the real and imaginary parts of the self-energy as shown in Figs. 2(c) and 2(d), respectively. The means that Σ'' possesses two humps corresponding to these two *kinks*. To understand the origin of the hump, we performed a fitting to Σ'' using multiple Eliashberg spectral functions [green dashed curves in Fig. 2(d)] following the Debye model [33]. The fitting resulted in two Debye frequencies 75 ± 6 and 195 ± 10 meV, which are very much in agreement with the energy positions of the *kinks* found from the band dispersion [Fig. 2(b)]. In addition to multiple Eliashberg spectral functions, we needed to add a Fermi liquid-type spectral function [red dashed curve in Fig. 2(d)], $\Sigma''(E) = \alpha + \beta E^2$, to properly fit Σ'' for the binding energies beyond 0.2 eV. Here, α represents the spectral width due to impurity scattering and β represents the strength of *e-e* correlations. The derived β value of 0.17 ± 0.03 eV^{-1} suggest weak *e-e* correlations in $K_{0.65}RhO_2$ compared with other high thermoelectric systems having a β value of 1.7 eV^{-1} [34]. We extracted a total coupling constant $\lambda = 2.7 \pm 0.3$ by fitting $\Sigma'(E)$ linearly with the formula of $\lambda = -\frac{d\Sigma'}{dE}$ near E_F, as shown in Fig. 2(c). Interestingly, this value is quite high compared with the coupling constant $\lambda = 0.4$ reported earlier for $K_{0.62}RhO_2$ [29]. The differing coupling constants could have originated from the additional band renormalization due to the high-energy anomaly at 195 meV. It is worth to mention here that such high value of coupling constants are also noticed from the high T_c superconductors [35]. In Ref. [35], a total coupling constant of $\lambda = 3.9$ has been reported for $(Bi, Pb)_2Sr_2CaCu_2O_{8+\delta}$ (Bi2212), with the *e*-ph interaction contribution of 2.3 and band renormalization contribution of 1.6. Following the same analogy, we subtracted the band renormalization contribution ($\lambda_b = \frac{v_b}{v_m} - 1 = 1.2 \pm 0.1$) from the total coupling constant to obtain an *e*-ph coupling constant of $\lambda_{e\text{-ph}} = 1.5 \pm 0.4$. This value, within the error bars, is in good agreement with the coupling constant independently obtained from the imaginary part of self-energy [35], $\lambda_{e\text{-ph}} = \frac{2\Sigma''(-\infty)}{\Omega_0 \pi} = 1.19 \pm 0.1$. Here $\Sigma''(-\infty) = 140$ meV and $\Omega_0 = 75 \pm 6$ meV. Further in supporting our observation, a coupling constant of $\lambda_{e\text{-ph}} = 1$ has been estimated for the multiboson-electron scattering in case of the misfit cobaltate, $[Bi_2Ba_2O_4][CoO_2]_2$ [34] which has the identical CoO_2 slabs to those in Na_xCoO_2.

In-plane electronic correlations are evaluated for the *AHL* plane as shown in Fig. 3. Figure 3(b) depicts representative band dispersions taken along the cuts *AH*, *AL*, and *AH'* by rotating $\Phi = -30^\circ$ to 30°, as demonstrated in Fig. 3(a). From Fig. 3(b), we can again observe multiple *kinks* from the all band dispersions almost at the same binding energy of 75 and 195 meV. We also estimated Fermi velocity v_F and group velocities v_m and v_b by fitting the band dispersions linearly in the binding-energy windows (0, 0.07), (0.1, 0.2), and (0.21, 0.3) eV, respectively. The calculated Fermi and group velocities vary sinusoidally with Φ as shown in Fig. 3(c), having maximum Fermi and group velocities, $v_F = 0.6 \pm 0.03$ eV Å, $v_m = 2.9 \pm 0.5$ eV Å, $v_b = 9.1 \pm 1$ eV Å along the *AH* direction and minimum Fermi and group velocities, $v_F = 0.52 \pm 0.02$ eV Å, $v_m = 2.1 \pm 0.3$ eV Å, $v_b = 3.5 \pm 0.5$ eV Å along the *AL* direction. These observations are consistent with the

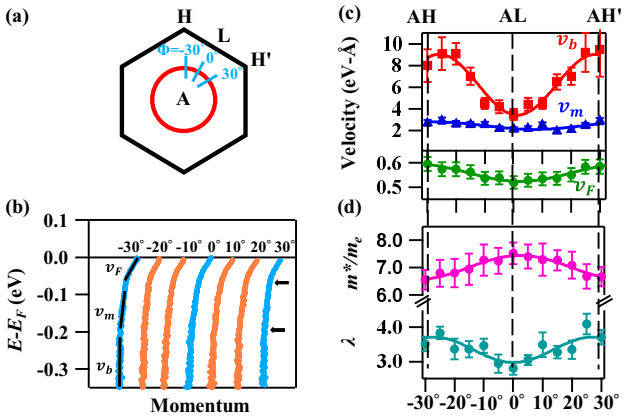

FIG. 3. (b) In-plane momentum-dependant band dispersions extracted from the EDMs taken along the cuts by varying Φ as shown in panel (a). (c) In-plane momentum dependant Fermi and group velocities extracted by fitting with linear function within the binding-energy windows as defined in panel (b). (d) In-plane momentum-dependent coupling constant λ and carrier effective mass m^*/m_e. In panels (c) and (d) the data are fit with cosine functions.

reported Φ-dependent Fermi velocities of Na_xCoO_2 [36]. The total coupling constant λ and the effective mass of the hole pocket, $m^* = \frac{\hbar k_F}{v_F}$, as a function of Φ are plotted in Fig. 3(d). From Fig. 3(d), we can notice that the coupling constant is maximum ($\lambda = 3.7$) for the electrons dispersing along *AH* and is minimum ($\lambda = 2.9$) for the electrons dispersing along *AL*. Furthermore, the effective mass is a minimum ($m^* = 6.5m_e$) along *AH* and is a maximum ($m^* = 7.4m_e$) along *AL*.

Next, electronic correlations have been evaluated for the out-of-plane momentum k_z direction, as shown in Fig. 4. Figure 4(a) depicts the Fermi surface (FS) map taken in the k_z-$k_\parallel$ plane by varying the photon energy $h\nu$ between 40 and 100 eV in steps of 4 eV. As can be seen from the k_z FS map, no change in the Fermi vector is noticed along the k_z direction, suggesting a nearly two-dimensional hole pocket without electron hopping in the k_z direction. In Fig. 4(b) we show representative imaginary part of the self-energy extracted from the EDMs measured with varying photon energies (k_z dependent). From each photon energy data, we consistently observe two humps in $\Sigma''(E)$, within the error-bars almost at the same binding energies of 75 and 195 meV. This is in very good agreement with *kinks* observed from the band dispersions extracted from corresponding photon energies [see Fig. 4(c)]. As discussed earlier, we could reasonably fit Σ'' at every photon energy using combined double-Eliashberg and Fermi-liquid-type spectral functions as shown in Fig. 4(b). We estimated β from the fittings and is plotted as a function of k_z ($h\nu$) as shown in Fig. 4(d). From Fig. 4(d), we notice that the *e-e* correlations hardly change along k_z (within the error bars). The estimated Fermi and group velocities are plotted in Fig. 4(e) as a function of k_z. From Fig. 4(e), we notice that all the velocities vary sinusoidally with k_z having minima at 60 and 92 eV and maxima at 43 and 75 eV photon energies. By considering the inner potential $V_0 = 12 \pm 2$ eV and using the formula $k_z = [\frac{2m}{\hbar^2}(V_0 + E_k)]^{1/2}$, we identify that the photon energies

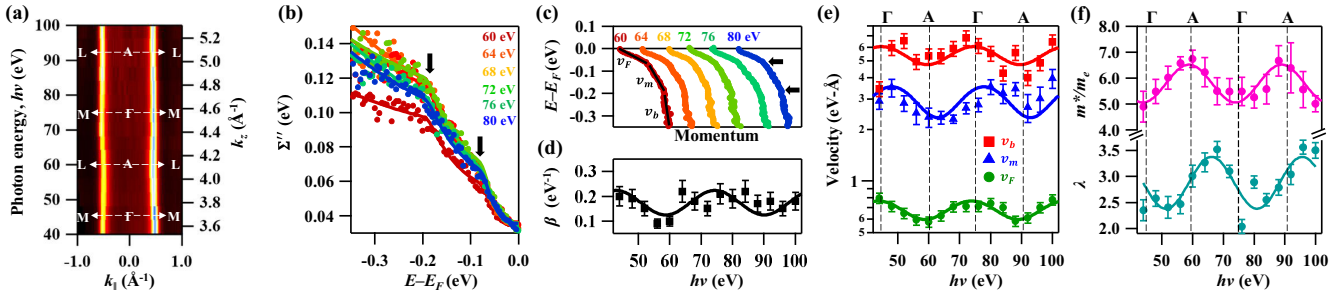

FIG. 4. (a) Out-of-plane Fermi-surface map taken in the k_z-$k_\parallel$ plane. (b) Representative k_z ($h\nu$) dependent imaginary part of the self-energy Σ''. (c) Representative k_z-dependent band dispersions. (d) k_z-dependent strength of electron-electron correlation extracted by fitting with Fermi-liquid-type spectral function (see text). (e) k_z-dependent Fermi and group velocities extracted by fitting with linear function within the binding energy window as shown in panel (c). (f) k_z-dependent coupling constant and carrier effective mass. In panels (d) and (e) the data are fit with cosine functions.

60 and 92 eV extract the bands from the AHL plane and the photon energies 45 and 75 eV extract the bands from the ΓMK plane. Thus, from Fig. 4(e), we can find that the Fermi velocity is minimum at the A point ($v_F = 0.6 \pm 0.04$ eV Å) and is maximum at the Γ point ($v_F = 0.76 \pm 0.06$ eV Å). Similarly, the group velocities v_m and v_b are minimum at $A(2.3 \pm 0.3, 4.76 \pm 0.5)$ eV Å and are maximum at Γ $(3.53 \pm 0.5, 6.06 \pm 0.8)$ eV Å. With the help of Fermi velocity and Fermi momentum, we estimated the effective mass of the hole pocket and plotted them as a function of k_z as shown in Fig. 4(f). A maximum effective mass is realized ($m^* = 6.51m_e$) at A, while a minimum effective mass is realized ($m^* = 5.06m_e$) at Γ. Furthermore, the k_z-dependent total coupling constants are plotted in Fig. 4(f). Note here that the maximum ($\lambda = 3.37$) and minimum ($\lambda = 2.38$) coupling constants are shifted by $h\nu = 5$ eV from the photon energy positions of the high-symmetry points, while still the photon energy difference between the two extrema is invariant (≈15 eV).

Since we completely extracted the in-plane and the out-of-plane Fermi sheets using ARPES, with the help of Luttinger's theorem [37], we are able to estimate the hole carrier density $n_h = 0.33 \pm 0.03$ per unit cell. This value is in very good agreement with the K deficiency percentage of the measured sample $K_{0.65(2)}RhO_2$ $(1 - x = 0.35 \pm 0.02)$ from the stoichiometric $KRhO_2$. Thus, the ARPES data confirm EDAX estimate of the chemical composition. As clearly demonstrated from our ARPES data, $K_{0.65}RhO_2$ possess two *kinks*. While the *kink* at 75 meV is consistent with the previous studies of Raman spectroscopy showing active $E_{1g} + E_{2g} + A_{1g}$ Raman modes at around 500 cm^{-1} from $K_{0.63}RhO_2$ [38], the high-energy *kink* at 195 meV is a finding of this study. Although the origin of low energy *kink* is reasonably understood, the origin of the HE *kink* is yet to be established. So far existing ARPES studies on these systems did not concentrate on the electronic correlations beyond 0.2 eV binding energy. Therefore, we are unable to compare the HE *kink* directly with previous ARPES studies of these systems. Nevertheless, as can be seen from Figs. 2 and 4, we can reasonably fit $\Sigma''(E)$ with multiple Debye frequencies at 75 and 195 meV. This suggests a plausible phononic origin for the HE *kink*. In fact, such an observation of bosonic scattering at higher energies has been noticed from Fe (100) at ≈160 meV [39], graphene at ≈200 meV [40], and cuprates at ≈350–400 meV below E_F [41,42]. The other existing mechanisms for the HE anomaly are the matrix element effects [43,44] and spin-fluctuations [45]. As observed in this study and reported in the literature, near the Fermi level only one band disperses from E_F down to a binding energy of 0.4 eV [29,46]. The same has been confirmed from the DFT calculations as well, especially in AHL plane [47]. Since the observed HE *kink* is at around 195 meV and only one band dispersion present within this energy range, it is highly unlikely that the HE *kink* originates from the matrix elements. Furthermore, the spin-fluctuations origin can be negated as the transport properties of $K_{0.65}RhO_2$ are nearly insensitive to the applied magnetic fields down to the lowest possible temperature [48]. Finally, as demonstrated in Fig. 1, the antiband crossing occur at ≈0.4 eV below E_F which shows no effect on the *kink* at 195 meV, ruling out the band-structure origin as well. Hence, the only convincing mechanism for the HE *kink* must be the electron-boson scattering at higher frequencies. But the present available literature on these systems is insufficient to confirm the same.

Our estimate of average Fermi velocity over the entire Brillouin zone $v_F = 0.62 \pm 0.04$ eV Å is far less than the Fermi velocity ($v_F = 0.96 \pm 0.02$ eV Å) reported earlier on $K_{0.62}RhO_2$ [29]. On the other hand, the average carrier effective mass estimated from this study, $m^* = 6.44m_e$ is a factor of 4.7 less than the effective mass reported for Na_xCoO_2 [27]. From this, we can conclude that $K_{0.65}RhO_2$ is relatively less correlated compared with Na_xCoO_2, but more correlated than what was thought earlier [29]. With the help of the average Fermi vector ($k_F = 0.51 \pm 0.02$ Å^{-1}) and Fermi velocity, we estimated the Seebeck coefficient using the Boltzmann theory [7,47], $S = \frac{2\pi^2 k_B^2 T}{3ek_F v_F}$, of 46 ± 5 μV/K at $T = 300$ K. This value is in excellent agrement with the Seebeck coefficient $S_{300K} = 46.3$ μV/K derived from the transport measurements on $K_{0.63}RhO_2$ [25]. We further verified the validity of Boltzmann theory in the present context by evaluating the Seebeck coefficient for $Na_{0.65}CoO_2$. Considering $k_F = 0.6$ Å^{-1} and averaged $v_F = 2.75$ eV Å from Ref. [31], we estimated the coefficient $S_{300K} = 89$ μV/K which is in very good agrement with the value of ≈90 μV/K obtained from the transport measurements on $Na_{0.67}CoO_2$ [49] and with the value of

≈85 μV/K obtained from DFT calculations on $Na_{0.67}CoO_2$ [50]. Thus, the Boltzmann theory is sufficient to understand the enhanced thermoelectric power in these systems.

IV. CONCLUSIONS

In conclusion, we systematically studied the low-energy electronic structure of $K_{0.65}RhO_2$ using ARPES technique and DFT calculations. Two *kinks* at the binding energies of 75 and 195 meV have been observed below E_F. As demonstrated above the strength of *e*-ph scattering, represented by the coupling constant λ, strongly depends on the in-plane and out-of-plane momenta. Most importantly, from this study we discover that the high-energy *kink* at 195 meV, leading to anomalous band renormalization near the Fermi level, plays a crucial role in obtaining the colossal thermoelectric power in these systems.

ACKNOWLEDGMENTS

S.C. acknowledges University Grants Commission (UGC), India for the Ph.D. fellowship. N.B.J. acknowledges support from the Prime Minister's Research Fellowship. A.N. acknowledges support from the startup grant (SG/MHRD-19-0001) at the Indian Institute of Science. S.A. and B.B. acknowledge financial support from Deutsche Forschungsgemeinschaft (DFG), Germany through the Projects No. 419457929 and No. 405940956. S.T. acknowledges financial support by Department of Science and Technology (DST), India through the INSPIRE-Faculty program (Grant No. IFA14 PH-86). S.T. acknowledges the financial support given by SNBNCBS through the Faculty Seed Grants program. The authors thank the Department of Science and Technology, India (SR/NM/Z-07/2015) for the financial support and Jawaharlal Nehru Centre for Advanced Scientific Research (JNCASR) for managing the project. The authors thank E.D.L. Reinks for fruitful discussions.

[1] D. J. Scalapino, The electron-phonon interaction and strong-coupling superconductors, in *Superconductivity*, edited by R. D. Parks (Marcel Dekker, NY, 1969), Chap. 10, pp. 449–560.

[2] G. R. Stewart, Heavy-fermion systems, Rev. Mod. Phys. **56**, 755 (1984).

[3] C.-X. Liu, S.-C. Zhang, and X.-L. Qi, The quantum anomalous Hall effect: Theory and experiment, Annu. Rev. Condens. Matter Phys. **7**, 301 (2016).

[4] R. A. de Groot, F. M. Mueller, P. G. van Engen, and K. H. J. Buschow, New Class of Materials: Half-Metallic Ferromagnets, Phys. Rev. Lett. **50**, 2024 (1983).

[5] N. F. Mott, The basis of the electron theory of metals, with special reference to the transition metals, Proc. Phys. Soc., London, Sect. A **62**, 416 (1949).

[6] T. Moriya and Y. Takahashi, Itinerant electron magnetism, Annu. Rev. Mater. Sci. **14**, 1 (1984).

[7] D. K. C. MacDonald, *Thermoelectricity: An Introduction to the Principles* (Dover Publications, Mineola, New York, 2006), pp. 1–65.

[8] J. A. Hertz and D. M. Edwards, Electron-magnon interactions in itinerant ferromagnetism. i. formal theory, J. Phys. F: Met. Phys. **3**, 2174 (1973).

[9] D. M. Edwards and J. A. Hertz, Electron-magnon interactions in itinerant ferromagnetism. II. strong ferromagnetism, J. Phys. F: Met. Phys. **3**, 2191 (1973).

[10] A. Lanzara, P. V. Bogdanov, X. J. Zhou, S. A. Kellar, D. L. Feng, E. D. Lu, T. Yoshida, H. Eisaki, A. Fujimori, K. Kishio, J.-I. Shimoyama, T. Noda, S. Uchida, Z. Hussain, and Z.-X. Shen, Evidence for ubiquitous strong electron–phonon coupling in high-temperature superconductors, Nature (London) **412**, 510 (2001).

[11] H. Wang, Y. Pei, A. D. LaLonde, and G. J. Snyder, Weak electron-phonon coupling contributing to high thermoelectric performance in N-type PbSe, Proc. Natl. Acad. Sci. USA **109**, 9705 (2012).

[12] J. van Elp, J. L. Wieland, H. Eskes, P. Kuiper, G. A. Sawatzky, F. M. F. de Groot, and T. S. Turner, Electronic structure of CoO, Li-doped CoO, and $LiCoO_2$, Phys. Rev. B **44**, 6090 (1991).

[13] I. Terasaki, Y. Sasago, and K. Uchinokura, Large thermoelectric power in $NaCo_2O_4$ single crystals, Phys. Rev. B **56**, R12685(R) (1997).

[14] J. Sugiyama, H. Nozaki, Y. Ikedo, K. Mukai, J. H. Brewer, E. J. Ansaldo, G. D. Morris, D. Andreica, A. Amato, T. Fujii, and A. Asamitsu, Static Magnetic Order in Metallic $K_{0.49}CoO_2$, Phys. Rev. Lett. **96**, 037206 (2006).

[15] S. Shibasaki, T. Nakano, I. Terasaki, K. Yubuta, and T. Kajitani, Transport properties of the layered Rh oxide $K_{0.49}RhO_2$, J. Phys.: Condens. Matter **22**, 115603 (2010).

[16] R. Schaak, T. Klimczuk, M. Foo, and R. Cava, Superconductivity Phase Diagram of $Na_xCoO_2 \cdot 1.3H_2O$, Nature (London) **424**, 527 (2003).

[17] M. Lee, L. Viciu, L. Li, Y. Wang, M. Foo, S. Watauchi, R. Pascal, R. Cava, and N. Ong, Large enhancement of the thermopower in Na_xCoO_2 at high Na doping, Nat. Mater. **5**, 537 (2006).

[18] L. M. Helme, A. T. Boothroyd, R. Coldea, D. Prabhakaran, D. A. Tennant, A. Hiess, and J. Kulda, Three-Dimensional Spin Fluctuations in $Na_{0.75}CoO_2$, Phys. Rev. Lett. **94**, 157206 (2005).

[19] S. P. Bayrakci, I. Mirebeau, P. Bourges, Y. Sidis, M. Enderle, J. Mesot, D. P. Chen, C. T. Lin, and B. Keimer, Magnetic Ordering and Spin Waves in $Na_{0.82}CoO_2$, Phys. Rev. Lett. **94**, 157205 (2005).

[20] M. L. Foo, Y. Wang, S. Watauchi, H. W. Zandbergen, T. He, R. J. Cava, and N. P. Ong, Charge Ordering, Commensurability, and Metallicity in the Phase Diagram of the Layered Na_xCoO_2, Phys. Rev. Lett. **92**, 247001 (2004).

[21] R. Okazaki, Y. Nishina, Y. Yasui, S. Shibasaki, and I. Terasaki, Optical study of the electronic structure and correlation effects in $K_{0.49}RhO_2$, Phys. Rev. B **84**, 075110 (2011).

[22] W. Koshibae and S. Maekawa, Effects of Spin and Orbital Degeneracy on the Thermopower of Strongly Correlated Systems, Phys. Rev. Lett. **87**, 236603 (2001).

[23] Y. Wang, N. Rogado, R. Cava, and N. Ong, Spin entropy as the likely source of enhanced thermopower in $Na_xCo_2O_4$, Nature (London) **423**, 425 (2003).

[24] A. Donkov, M. M. Korshunov, I. Eremin, P. Lemmens, V. Gnezdilov, F. C. Chou, and C. T. Lin, Electron-phonon interaction in the lamellar cobaltate Na_xCoO_2, Phys. Rev. B **77**, 100504(R) (2008).

[25] S. H. Yao, B. B. Zhang, J. Zhou, Y. B. Chen, S. T. Zhang, Z. B. Gu, S. T. Dong, and Y. F. Chen, Structure and physical properties of $K_{0.63}RhO_2$ single crystals, AIP Adv. **2**, 042140 (2012).

[26] Y. Saeed, N. Singh, and U. Schwingenschlögl, Colossal thermoelectric power factor in $K_{7/8}RhO_2$, Adv. Funct. Mater. **22**, 2792 (2012).

[27] M. Z. Hasan, Y.-D. Chuang, D. Qian, Y. W. Li, Y. Kong, A. P. Kuprin, A. V. Fedorov, R. Kimmerling, E. Rotenberg, K. Rossnagel, Z. Hussain, H. Koh, N. S. Rogado, M. L. Foo, and R. J. Cava, Fermi Surface and Quasiparticle Dynamics of $Na_{0.7}CoO_2$ Investigated by Angle-Resolved Photoemission Spectroscopy, Phys. Rev. Lett. **92**, 246402 (2004).

[28] H.-B. Yang, Z.-H. Pan, A. K. P. Sekharan, T. Sato, S. Souma, T. Takahashi, R. Jin, B. C. Sales, D. Mandrus, A. V. Fedorov, Z. Wang, and H. Ding, Fermi Surface Evolution and Luttinger Theorem in Na_xCoO_2: A Systematic Photoemission Study, Phys. Rev. Lett. **95**, 146401 (2005).

[29] S.-D. Chen, Y. He, A. Zong, Y. Zhang, M. Hashimoto, B.-B. Zhang, S.-H. Yao, Y.-B. Chen, J. Zhou, Y.-F. Chen, S.-K. Mo, Z. Hussain, D. Lu, and Z.-X. Shen, Large thermopower from dressed quasiparticles in the layered cobaltates and rhodates, Phys. Rev. B **96**, 081109(R) (2017).

[30] See supplemental material at http://link.aps.org/supplemental/10.1103/PhysRevMaterials.5.055402 for experimental methods, additional ARPES data, DFT calculations, EDAX and XRD data.

[31] T. Arakane, T. Sato, T. Takahashi, T. Fujii, and A. Asamitsu, Angle-resolved photoemission study of the doping evolution of a three-dimensional Fermi surface in Na_xCoO_2, New J. Phys. **13**, 043021 (2011).

[32] Y. Okamoto, R. Matsumoto, T. Yagihara, C. Iwai, K. Miyoshi, J. Takeuchi, K. Horiba, M. Kobayashi, K. Ono, H. Kumigashira, N. L. Saini, and T. Mizokawa, Electronic structure and polar catastrophe at the surface of Li_xCoO_2 studied by angle-resolved photoemission spectroscopy, Phys. Rev. B **96**, 125147 (2017).

[33] F. Reinert and S. Hüfner, Photoemission Spectroscopy with Very High Energy Resolution: Studying the Influence of Electronic Correlations on the Millielectronvolt Scale, in *Very High Resolution Photoelectron Spectroscopy* (Springer, Berlin, Heidelberg, 2007), pp. 13–53.

[34] A. Nicolaou, V. Brouet, M. Zacchigna, I. Vobornik, A. Tejeda, A. Taleb-Ibrahimi, P. Le Fèvre, F. Bertran, S. Hébert, H. Muguerra, and D. Grebille, Experimental Study of the Incoherent Spectral Weight in the Photoemission Spectra of the Misfit Cobaltate $[Bi_2Ba_2\mathbf{O}_4][CoO_2]_2$, Phys. Rev. Lett. **104**, 056403 (2010).

[35] J. Fink, S. Borisenko, A. Kordyuk, A. Koitzsch, J. Geck, V. Zabolotnyy, M. Knupfer, B. Büchner, and H. Berger, Dressing of the Charge Carriers in High-T_c Superconductors, in *Very High Resolution Photoelectron Spectroscopy*, edited by S. Hüffner (Springer, Berlin, Heidelberg, 2007), pp. 295–325.

[36] J. Geck, S. V. Borisenko, H. Berger, H. Eschrig, J. Fink, M. Knupfer, K. Koepernik, A. Koitzsch, A. A. Kordyuk, V. B. Zabolotnyy, and B. Büchner, Anomalous Quasiparticle Renormalization in $Na_{0.73}CoO_2$: Role of Interorbital Interactions and Magnetic Correlations, Phys. Rev. Lett. **99**, 046403 (2007).

[37] J. M. Luttinger, Fermi surface and some simple equilibrium properties of a system of interacting fermions, Phys. Rev. **119**, 1153 (1960).

[38] B.-B. Zhang, N. Zhang, S.-T. Dong, Y. Lv, Y. B. Chen, S. Yao, S.-T. Zhang, Z.-B. Gu, J. Zhou, I. Guedes, D. Yu, and Y.-F. Chen, Lattice dynamics of K_xRhO_2 single crystals, AIP Adv. **5**, 087111 (2015).

[39] J. Schäfer, D. Schrupp, E. Rotenberg, K. Rossnagel, H. Koh, P. Blaha, and R. Claessen, Electronic Quasiparticle Renormalization on the Spin Wave Energy Scale, Phys. Rev. Lett. **92**, 097205 (2004).

[40] F. Mazzola, J. W. Wells, R. Yakimova, S. Ulstrup, J. A. Miwa, R. Balog, M. Bianchi, M. Leandersson, J. Adell, P. Hofmann, and T. Balasubramanian, Kinks in the σ Band of Graphene Induced by Electron-Phonon Coupling, Phys. Rev. Lett. **111**, 216806 (2013).

[41] T. Valla, T. E. Kidd, W.-G. Yin, G. D. Gu, P. D. Johnson, Z.-H. Pan, and A. V. Fedorov, High-Energy Kink Observed in the Electron Dispersion of High-Temperature Cuprate Superconductors, Phys. Rev. Lett. **98**, 167003 (2007).

[42] D. S. Inosov, J. Fink, A. A. Kordyuk, S. V. Borisenko, V. B. Zabolotnyy, R. Schuster, M. Knupfer, B. Büchner, R. Follath, H. A. Dürr, W. Eberhardt, V. Hinkov, B. Keimer, and H. Berger, Momentum and Energy Dependence of the Anomalous High-Energy Dispersion in the Electronic Structure of High Temperature Superconductors, Phys. Rev. Lett. **99**, 237002 (2007).

[43] S. Basak, T. Das, H. Lin, J. Nieminen, M. Lindroos, R. S. Markiewicz, and A. Bansil, Origin of the high-energy kink in the photoemission spectrum of the high-temperature superconductor $Bi_2Sr_2CaCu_2O_8$, Phys. Rev. B **80**, 214520 (2009).

[44] E. D. L. Rienks, M. Ärrälä, M. Lindroos, F. Roth, W. Tabis, G. Yu, M. Greven, and J. Fink, High-Energy Anomaly in the Angle-Resolved Photoemission Spectra of $Nd_{2-x}Ce_xCuO_4$: Evidence for a Matrix Element Effect, Phys. Rev. Lett. **113**, 137001 (2014).

[45] J. Graf, G.-H. Gweon, K. McElroy, S. Y. Zhou, C. Jozwiak, E. Rotenberg, A. Bill, T. Sasagawa, H. Eisaki, S. Uchida, H. Takagi, D.-H. Lee, and A. Lanzara, Universal High Energy Anomaly in the Angle-Resolved Photoemission Spectra of High Temperature Superconductors: Possible Evidence of Spinon and Holon Branches, Phys. Rev. Lett. **98**, 067004 (2007).

[46] H. W. Ou, J. F. Zhao, Y. Zhang, B. P. Xie, D. W. Shen, Y. Zhu, Z. Q. Yang, J. G. Che, X. G. Luo, X. H. Chen, M. Arita, K. Shimada, H. Namatame, M. Taniguchi, C. M. Cheng, K. D. Tsuei, and D. L. Feng, Novel Electronic Structure Induced by a Highly Strained Oxide Interface with Incommensurate Crystal Fields, Phys. Rev. Lett. **102**, 026806 (2009).

[47] D. J. Singh, Electronic structure of $NaCo_2O_4$, Phys. Rev. B **61**, 13397 (2000).

[48] B.-B. Zhang, S.-T. Dong, S.-H. Yao, Y. B. Chen, S.-T. Zhang, Z.-B. Gu, J. Zhou, M.-H. Lu, Y.-F. Chen, and Y. G. Shi, Electrical, magnetic, and magneto-electrical properties in quasi-two-dimensional $K_{0.58}RhO_2$ single crystals doped with rare-earth elements, Appl. Phys. Lett. **105**, 062408 (2014).

[49] M. S. Pandiyan, Ph.D. thesis, University of London, 2013 (unpublished).

[50] D. J. Singh and D. Kasinathan, Thermoelectric properties of Na_xCoO_2 and prospects for other oxide thermoelectrics, J. Electron. Mater. **36**, 736 (2007).